View metadata, citation and similar papers at core.ac.uk

brought to you by CORE

provided by IR@NPL

RSC Advances

PAPER

View Article Online
View Journal | View Issue

Published on 07 April 2014. Downloaded by National Institute of Technology - Rourkela on 17/10/2014 07:27:03.

Cite this: *RSC Adv.*, 2014, **4**, 22840

# Room temperature lead-free relaxor–antiferroelectric electroceramics for energy storage applications†

Hitesh Borkar,[a] V. N. Singh,[a] B. P. Singh,[a] M. Tomar,[b] Vinay Gupta[c] and Ashok Kumar*[a]

Received 6th January 2014
Accepted 3rd April 2014

DOI: 10.1039/c4ra00094c

www.rsc.org/advances

Round the globe, scientific communities have been searching for new materials for "green" energy, producing efficiently both high power as well as high energy density. Relaxor ferroelectrics (RFEs) have shown immense potential to achieve this goal. We report fabrication of $[Na_{0.42}Bi_{0.44}Al_{0.06}Ba_{0.08}]TiO_3$ (NBAT–BT)], a lead-free-relaxor antiferroelectric ceramic, *via* a conventional solid-state reaction method. A small fraction of trivalent cations ($Al^{3+}$) doping at $Na^{1+}/Bi^{3+}$ sites develop anti-polar phase in the ferroelectric matrix which in turn changes its functional properties. Rietveld refinement suggests the existence of both tetragonal and rhombohedral phases which is well supported by *d*-spacing values obtained in high resolution transmission electron microscopy (HRTEM) studies. Elemental analysis confirms the stoichiometry of the system and matches the starting composition well within the experimental uncertainty (±10%) of secondary electron microscopy (SEM) and HRTEM data. Raman spectra suggest the substitution of $Al^{3+}$ cation at an A-site sublattice. Temperature-dependent dielectric spectra show frequency dependent dielectric dispersion near 80–110 °C, high dielectric loss at high probing frequency, and a non-linear Vogel–Fulcher relation, substantiating the relaxor–antiferroelectric (r-AFE) nature of NBAT–BT. A second order diffuse anti/ferro-electric to paraelectric phase transition near 230–240 °C was observed which follows a modified Curie–Weiss law. The energy density was calculated from polarization–electric field (*P*–*E*) loops and dielectric–electric field ($\varepsilon$–*E*) plot. The values were in the range of 0.4–0.6 J cm$^{-3}$, which is reasonably good for bulk polar material. NBAT–BT shows a much thinner AFE hysteresis above its relaxor FE phase transition; that favors the enhanced energy storage capacity at elevated temperature in the depolarized paraelectric region.

## Introduction

Nowadays green energy generation and storage materials and devices are a major growth area of research and technology. Dielectric capacitors are well-known for their high power density and discharge capability (time constant ~ μs). Among the dielectrics, ferroelectrics usually possess higher dielectric constants and fast discharge time (~ns) that make them suitable candidates for high energy density storage applications.[1,2] At present, the energy density of dielectrics/ferroelectrics materials is poor compared to supercapacitors and the Li-ion batteries.[3] The low energy density of polar dielectrics is due to low breakdown field, high dielectric saturation, square hysteresis (dielectric loss) and large leakage current under the application of an electric field.[4,5] Short range order (SRO) relaxors embedded in an anti-ferroelectric matrix have an enormous potential in designing new polar dielectrics for high energy storage applications due to their slim polarization–electric field (*P*–*E*) hysteresis. Anti-ferroelectrics have linear and non-linear hysteresis (in *E*) that yield the largest energy storage area in *P*–*E* hysteresis in any polar dielectrics.[6] This indicates that an anti-ferroelectric matrix embedded with polar-nano-regions (PNRs) (relaxor–antiferroelectric) are suitable candidates for moderate power and energy-density applications. Such a system may allow us to understand new capacitor materials having high dielectric constant and energy storage capacity. Lead-based relaxor antiferroelectric PLZT (lead–lanthanum–zirconate–titanate) thick films show a high energy density (up to 58.1 J cm$^{-3}$ at 2.8 MV cm$^{-1}$). However, the environmental issues and regulations to ban toxic materials by several countries are forcing the development of lead-free (non-toxic) research.[7,8]

The direct way to calculate the energy density and energy storage capacity per unit volume of material is as follows:

$$U = \int E\mathrm{d}D = \int E\mathrm{d}P \quad (1)$$

[a]*CSIR-National Physical Laboratory, Dr. K. S. Krishnan Marg, New Delhi 110012, India. E-mail: ashok553@nplindia.org*

[b]*Department of Physics, Miranda House, University of Delhi, Delhi 110007, India*

[c]*Department of Physics and Astrophysics, University of Delhi, Delhi 110007, India*

† Electronic supplementary information (ESI) available. See DOI: 10.1039/c4ra00094c



This journal is © The Royal Society of Chemistry 2014

Published on 07 April 2014. Downloaded by National Institute of Technology - Rourkela on 17/10/2014 07:27:03.

where $D = \varepsilon_0 E + P$, since polarization of ferroelectric dielectrics is very high so $D \approx P$.

$$\overline{U} = \frac{1}{2}\frac{CV^2}{\text{volume}} = \frac{1}{2}\frac{\varepsilon\varepsilon_0 A {E_b}^2 {t_{die}}^2}{t_{die} A t_{die}} = \frac{1}{2}\varepsilon\varepsilon_0\eta^2 {E_b}^2 \quad [\text{J cm}^{-3}] \qquad (2)$$

where $C$ is capacitance; $E$, applied electric field; $P$, polarization; $V$, voltage; $\varepsilon$, dielectric constant of the material, $\varepsilon_0$ dielectric constant of vacuum, and $E_b$ breakdown field. The dielectric is susceptible to breakdown under the application of constant high external field. To avoid any premature breakdown of the capacitor, it is advisable to use an external field almost half of the breakdown field, *i.e.*, $V = \eta V_b$ $(0 < \eta < 1)$.[9]

The lead free $(1-x)(Na_{0.50}Bi_{0.50})TiO_{3-x}BaTiO_3$ (NBT–BT) system is well known for its excellent piezoelectric properties, several structural phase transitions, large variation in functional properties due to composition tunability, and coexistence of relaxor–polar and antipolar phases.[10–14] The NBT–BT system illustrates depolarization properties [that is, transition of ferroelectric FE to AFE-like phases] in the temperature range of 100 to 190 °C depending on the composition of BT near the morphotropic phase boundary (MPB).[15–17] The rhombohedral (FE) to high-temperature tetragonal diffuse phase transition (220–320 °C) is achieved *via* an intermediate AFE-like phase transition. Ma *et al.* showed the presence of nano-size short-range polar-regions for the compositions $(0.07 \leq x \leq 0.09)$ that lead to the relaxor–AFE phase boundary. Recently they also established a new phase boundary in NBT–BT measuring the precise positions of oxygen octahedral tilting in multi-domain perovskite ferroelectrics using electron diffraction analysis.[18] Another aspect, non-stoichiometry, is equally important in determining piezoelectric properties and depolarization temperatures. Many research groups have extensively studied the non-stoichiometry–microstructure–property relationship.[19–25] In general, it has been accepted that $Na^+$ cation deficiencies and excess Bi cations lead to a decrease in depolarization temperature and develop the AFE-like micropolar regions in the ferroelectric matrix. The ratio of A-site cations ($Na^+$ and $Bi^{3+}$) was always considered as unity; however, in reality it is very hard to maintain such a ratio, due to the volatile nature of both Na- and Bi-cations. Guo *et al.* have carried out an extensive study on the compositional modulation of the NBT–BT system and have shown that an AFE-like phase can be induced at an ambient temperature.[26]

Lead-based relaxor/anti-ferroelectrics have been thoroughly investigated for high energy density applications and have shown a high energy storage capacity.[27] Polymer relaxor ferroelectric thin films show a high energy density (10–25 J cm$^{-3}$) with a very fast discharge capacity.[3] Ceramic–polymer and ceramic–glass composite systems are also potential candidates for high energy density capacitors due to their high breakdown strength and low dielectric saturation.[28–30] Polar or non-polar multilayers and superlattice thin films have been investigated by most material science techniques and have also shown tremendous potential in energy applications with a suitable design of the polar–nonpolar layers.[3]

In this paper, we report the effect of $Al^{3+}$ cation (valance state (+3) of A-site) substitution on the relaxor–AFE properties of NBAT–BT. A minimum $Al^{3+}$ cation percentage is incorporated in the system to avoid any pyrochlore or impurity phase. The microstructure–property relationship is discussed in the context of its ability to store energy.

## Experimental

Polycrystalline ceramic samples of $(Na_{0.42}Bi_{0.44}Al_{0.06}Ba_{0.08})TiO_3$ (initial precursor compositions $(Na_{0.43}Bi_{0.43}Al_{0.06})TiO_3$–$Ba_{0.08}TiO_3$) were prepared by conventional solid state reaction techniques. The high purity (~99.9%) initial precursors $Na_2CO_3$, $BaCO_3$, $Bi_2O_3$, $TiO_2$ and $Al_2O_3$ (Sigma Aldrich) were mixed at ambient conditions and then homogenously blended with IPA (isopropyl alcohol), using agate mortar–pestle grinding for 2 h. The mixed precursors were first calcined at an optimized temperature of 1000 °C for about 4 h in a high purity alumina crucible. Calcined powder was reground and then mixed with a binder (polyvinyl alcohol) in order to prepare the circular disc-shaped pellets. The average diameter and thickness of the pellets were 13 mm and 1–1.5 mm, prepared under uniaxial pressure of 5–6 tons per square inch. The prepared pellets were subsequently sintered at an optimized temperature of 1200 °C for 8 h to achieve the 92–95% of theoretical density. A room temperature X-ray diffraction pattern was taken using CuK$\alpha$ radiation ($\lambda$= 1.5460 Å, Bruker D8 Advance) over a wide range of Bragg angle ($20° < \theta < 80°$) to identify the structure and phase purity of the sintered ceramic pellets.

Grain growth, surface morphology, and elemental analysis on sintered pellets were carried out using a scanning electron microscope (SEM, Zeiss EVO MA-10). Crystal structure, atom positions in lattice planes, grain orientations, and size were determined by using a Technai G20-stwin, 300 kV, High Resolution Transmission Electron Microscope (HRTEM). To measure the electrical properties, metal–insulator–metal capacitor structures were prepared using the silver paint coating on both sides of the ceramic pellets. Temperature-dependent dielectric measurements were carried out on metallized pellets at various frequencies (1 kHz to 1 MHz) and temperatures using an LCR meter (4200-SCS Analyzer) at an oscillating amplitude of 0.5 V. Ferroelectric *P–E* hysteresis loops and leakage current were measured by using a Radiant Ferroelectric Tester. Room temperature Raman studies were carried out using a Renishaw inVia Reflex Raman spectrometer, UK (with an excitation source of 514.5 nm) with a resolution of less than 1.0 cm$^{-1}$.

## Results and discussion

### A. Crystal structure

Rietveld refinement on the unpoled X-ray diffraction data were tested for the determination of the amount of both the tetragonal (space group *P4mm*) and rhombohedral (space group *R3c*) crystal structures as reported earlier for the MPB of the NBT–BT system.[31] (Na, Bi, Al, Ba) and Ti ions were added to A and B sites of $ABO_3$ perovskite, respectively, using the occupancy constraint relationship $n_{A2+} = 1 - n_{B4+}$. The observed diffraction peaks were simulated with a pseudo-Voigt profile function. The normal procedures for the Rietveld refinement have been

Published on 07 April 2014. Downloaded by National Institute of Technology - Rourkela on 17/10/2014 07:27:03.

followed for the simulation of experimental X-ray data. Anisotropic values of atomic (thermal) displacement (Debye–Waller factor) parameters were obtained in the stable and best fit.[32] The reliability factors for the rhombohedral crystal structure are $R_p$ = 9.43%, $R_{wp}$ = 12.1%, $\chi^2$ = 2.89, $R_{exp}$ = 6.98%, $R_{Bragg}$ = 5.46% and lattice constants ($a$ = 5.5173 Å, $b$= 5.5173 Å, $c$= 13.4722 Å) and for tetragonal are $R_p$ = 7.61%, $R_{wp}$ = 10.4%, $\chi^2$ = 2.09, $R_{exp}$ = 6.97%, $R_{Bragg}$ = 3.94%, and lattice constants ($a$ = 3.8964 Å, $b$= 3.8964 Å, $c$= 3.9255 Å). The reliability factors were in good agreement with those reported by Wook *et al.*[31] Fig. 1(a) & (b) show a very good agreement between the experimental and simulated profile data for the above mentioned reliability factor values. All the prominent Bragg peaks were successfully indexed for both the crystal structures. The incorporation of a very small fraction of $Al^{3+}$ cations hardly affects the lattice parameters, and it is not easy to detect the elemental compositions and crystallographic positions with low resolution XRD and HRTEM results. Fractional atomic coordinates, positions, occupancies and other fitted parameters are presented in Table 1. The *d*-spacing of different planes calculated using the HRTEM data matches well with the tetragonal–rhombohedral crystal structure. The difference in the *d*-spacing for both the systems was detectable only after two decimal points of *d*-spacing data (<1%). It would be unwise to report the exact lattice planes for either system with the given HRTEM image resolution. XRD analysis was carried out on unpoled-polycrystalline samples to obtain the ratio of both crystal phases. The results obtained from the refined intensity of the coexisting rhombohedral (r-phase) and tetragonal phases (t-phase) suggests that NBAT–BT is composed of 48(± 5)% r-phase and 52 (±5)% t-phase. The existence of twin boundaries and their separate phases can also be seen in the HRTEM image of the (110) plane with their fast Fourier transformation (FFT) as depicted in Fig. 3. The intensities of both phases are slightly different from each other over a large area of the crystal surface confirming the presence of both phases and its distribution throughout the matrix.

Table 1 Simulation data of the Rietveld analysis for two space groups (*R*3*c* and *P*4*mm*) and crystal systems[a,b]

| Phases | Atoms | *X* | *Y* | *Z* |
|---|---|---|---|---|
| Tetragonal *P*4*mm* | Bi | 0.00 | 0.00 | 4.27949 |
| | Ba | 0.00 | 0.00 | 4.65655 |
| | Na | 0.00 | 0.00 | 4.95192 |
| | Al | 0.00 | 0.00 | 4.95192 |
| | Ti | 0.50 | 0.50 | −5.35526 |
| | O1 | 0.50 | 0.50 | 6.46282 |
| | O2 | 0.50 | 0.00 | 5.58466 |
| Rhombohedral *R*3*c* | Bi | 0.00 | 0.00 | 0.63378 |
| | Ba | 0.00 | 0.00 | 0.63378 |
| | Na | 0.00 | 0.00 | 0.63378 |
| | Al | 0.00 | 0.00 | 0.63378 |
| | Ti | 0.00 | 0.00 | 0.39033 |
| | O | −0.05406 | 1.46715 | 1.11697 |

[a] Reliability factors are $R_p$ = 7.61%, $R_{wp}$ = 10.4%, $\chi^2$ = 2.09, $R_{exp}$ = 6.97% and $R_{Bragg}$ = 3.94%. [b] Reliability factors are $R_p$ = 9.43%, $R_{wp}$ = 12.1%, $\chi^2$ = 2.89, $R_{exp}$ = 6.98% and $R_{Bragg}$ = 5.46%.

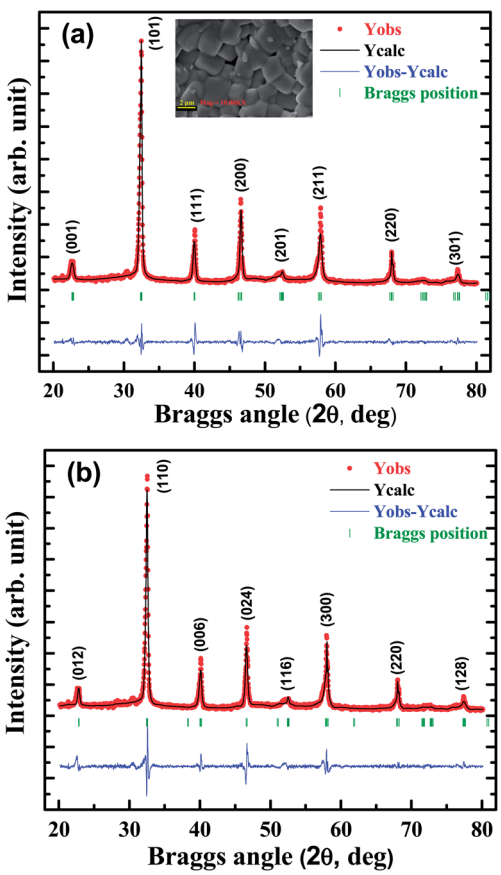


Fig. 1 (a) shows the Rietveld fitting of NBAT–BT XRD patterns with tetragonal crystal structure (space group *P*4*mm*) and (b) rhombohedral crystal structure (space group *R*3*c*); SEM image is given in the inset (a).

## B. Morphology, size and *d*-spacing of crystal

The surface morphology and grain growth can be seen from the SEM image (inset of Fig. 1(a)) of the as-grown pellets. They indicate fine square grains with an average size of 1–5 μm. These grains are highly packed with little porosity. EDAX analysis for the appropriate elemental composition was carried out on large areas of the pellets and on individual grains. A reliable matching elemental ratio was obtained between precursor and the final product. The final elemental ratio is given in Table 2. To better understand the microstructure–property relation, electron diffraction patterns were taken on various sintered ceramic grains. These grains were obtained from mechanically milled powder of the sintered pellets. The ultrasonicated dispersions of fine particles were put on carbon-coated copper grids for HRTEM study. The TEM results from the representative grains are shown in Fig. 2(a)–(f). Fig. 2(a) shows the fine nano-grains surrounded by larger grains >100 nm. To check the real distribution of the fine grains, TEM imaging was carried out on different particles of the NBAT–BT. Each time it showed an uneven distribution of nanoparticles in the matrix. Fig. 2(b) elucidates the small ordered regions (different contrast compared to the surroundings) in the matrix; which may

 This journal is © The Royal Society of Chemistry 2014

Published on 07 April 2014. Downloaded by National Institute of Technology - Rourkela on 17/10/2014 07:27:03.

Table 2 Stoichiometric details of the A-site elements for the NBAT–BT crystal system

| Elements at A-site | Percentage of initial elemental compositions | Observed elemental compositions from SEM & HRTEM (±10% uncertainty) |
|---|---|---|
| Na | 0.43 | 0.42 |
| Bi | 0.43 | 0.44 |
| Ba | 0.08 | 0.08 |
| Al | 0.06 | 0.06 |

represent the PNRs, responsible for large dielectric dispersion near room temperature. The *d*-spacing for both the crystal systems were imaged for different parts of the grains in HRTEM studies. Fig. 2(c)–(f) represents different lattice planes of the NBAT–BT crystal that matched well with the *d*-spacing obtained for the tetragonal crystal structure from the X-ray data (Rietveld analysis). The observed planes for both crystal systems vary only in the third decimal. This is hard to distinguish form the present HRTEM image resolutions. However, one point is clear from all these TEM images: these planes are not single crystalline in nature; they possess polycrystalline contrast, chemical inhomogeneities, discontinuity, disorder, and a mixture of long and short range ordering. These observations support the relaxor–AFE character of the samples. Therefore, a relaxor–AFE phase and the coexistence of a rhombohedral–tetragonal phase at room temperature are proposed near the MPB with substitution of a small amount of trivalent cations. Fig. 3(a) and (b) shows the FFT and inverse FFT (IFFT) images of NBAT–BT polycrystals. FFT and IFFT analysis were carried out on the large area HRTEM image which shows the co-existence of both the phases with a slight difference in their crystallographic plane intensities and positions. The presence of both t-phase and r-phase (101) and (110) planes can be seen from the Fig. 3, respectively. Atomic contrast on various atomic planes and small regions with different microstructure intensity (circled on the TEM image) can be seen in Fig. 3(b) suggesting the existence of chemical inhomogeneity in the systems supporting the microstructure–property relationship. HRTEM images also revealed that some crystal areas having a large number of twin boundaries promote the formation of twin phases (as highlighted by the transparent lines).

### C. Raman spectroscopy

Raman spectroscopy is a versatile tool for the detection of subtle structural distortions, local defects, compositional inhomogeneity, and different ordering states in perovskite structures. Raman spectra of the NBAT–BT are analyzed using the damped harmonic oscillator model (DHO).[33] The observed vibrational modes are analyzed and fitted with the spectral response function.

$$S(\nu) = \sum_i \frac{\chi_{0i}\Gamma_i {\nu_{0i}}^2 \nu}{(\nu^2 - {\nu_{0i}}^2) + {\Gamma_i}^2 \nu^2} F(\nu, T) \quad (3)$$

where $F(\nu, T) = [n(\nu) + 1]$ (Stokes scattering) and $n(\nu) = [\exp(h\nu/\kappa T) - 1]^{-1}$. The parameters in eqn (1) amplitude $\chi_0$ (in

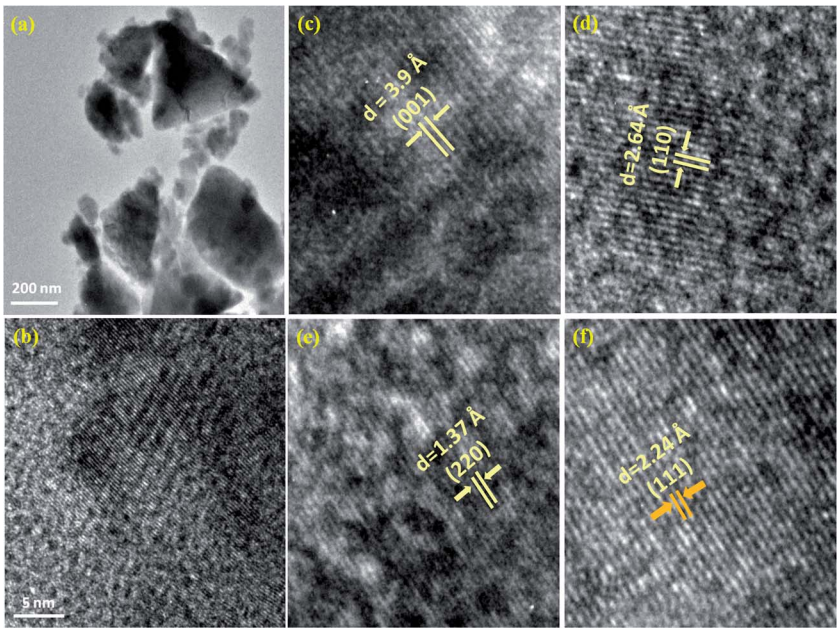


Fig. 2 (a–f) HRTEM images of NBAT–BT crystal and lattice planes, (a) HRTEM images of NBAT–BT nano- and micro-crystals, (b) ordered PNRs in the AFE matrix, (c–f) *d*-spacing of crystal planes (001), (110), (220), (111) respectively.

Published on 07 April 2014. Downloaded by National Institute of Technology - Rourkela on 17/10/2014 07:27:03.

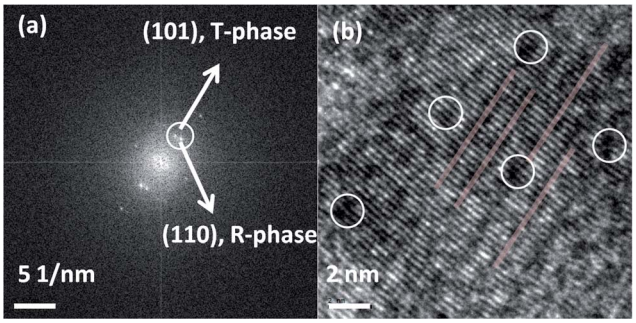


Fig. 3 (a) FFT image of the (101) and (110) planes of the r-phase and t-phase, (b) IFFT image of the same FFT showing the presence of twin phase boundaries and various SROs.

arbitrary units), the mode frequency $\nu_0$, the damping constant $\Gamma$, and the temperature $T$, describe each phonon mode as a damped harmonic oscillator. Fig. 4(a)–(d) show the Raman spectra and their DHO model fitting over large frequency regions of NBAT–BT ceramics. The intensities of low frequency vibrational modes are six times higher than the high frequency modes that make it difficult for DHO to fit all the Raman modes with a single frequency window. Group theory predicts $4A_1$(IR, R) + 9E(IR, R) optical modes for the rhombohedral *R3c* phase, and 7(IR + R) + 1R modes for the tetragonal *P4mm* phase.[34] Fig. 4(a) illustrates the Raman spectra of NBAT–BT electroceramics which is in accordance with the previous reported data on NBT–BT.[35,36] In general, Raman bands are relatively broad due to chemical inhomogeneity, overlapping different Raman vibrational modes, and chemical potential of four cations with different atomic mass and radii at the A-site sublattice. Fig. 4(b) and (c) shows three Raman active modes at 116 $cm^{-1}$, 153 $cm^{-1}$, and 183 $cm^{-1}$ below the 200 wavenumber. A low frequency 96 $cm^{-1}$ mode was observed, however, it cannot be considered trustworthy due to the experimental limitations of the Renishaw inVia Reflex Raman spectrometer. The variation in the intensity of the various peaks below 200 $cm^{-1}$ could be a result of the substitution of Al(3+) at an A-site sublattice. The presence of four cations (Al/Na/Bi/Ba) causes difficulty in analyzing the mass and radii effects on low frequency Raman modes. The overlapped Raman spectra of the specimens is mainly due to the random distribution of Na, Al, Bi and Ba cations breaks the $k = 0$ selection rule and permits phonons from the entire Brillouin zone to become Raman active. Four Raman active modes were observed for the medium frequency range (250–550 $cm^{-1}$) which represent the oxygen ion vibration with different A and B-site cations and also due to dielectric leakage.[36] The high frequency Raman modes in the region of 600–900 $cm^{-1}$ have been attributed to B-site sublattice (Ti–O–Ti stretching modes), in which the vibration around 600–700 $cm^{-1}$ corresponds to edge shared octahedral, 748 $cm^{-1}$ to corner sharing octahedral, and at 805/859 $cm^{-1}$ short Ti–O bonds in the distorted $TiO_6$ octahedral. These bands match the vibration of pure NBT–BT ceramics near the morphotropic phase boundaries (MPB). The band positions of high frequency Raman modes indicate the negligible effect of the Al doping at the B-site. Low frequency band positions and intensity indicate a substantial influence of the Al cation at the A-site sublattice.

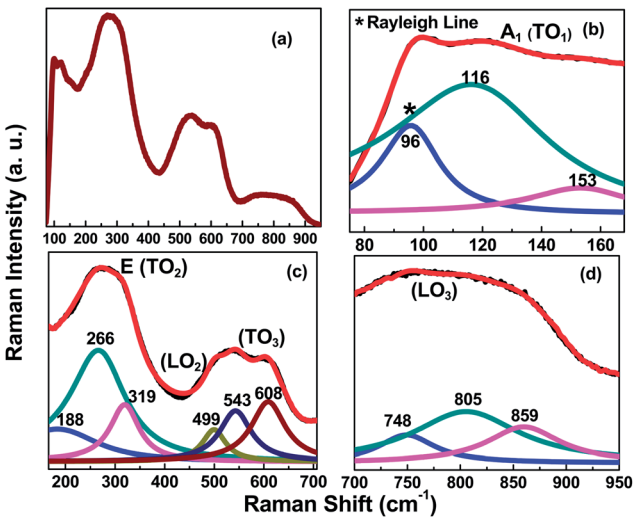


Fig. 4 (a–d) Raman spectra of NBAT–BT system with DHO model fitting (b) low (c) medium (d) high frequency regions.

### D. Dielectric and tangent loss spectroscopy

Fig. 5(a) and (b) show the dielectric constant ($\varepsilon$) and tangent loss (tan $\delta$) data as functions of temperature at different frequencies. Two well-defined $\varepsilon$ and tan $\delta$ anomalies can be seen near 80–120 °C and 240 °C, respectively. The first phase transition shows a well-defined $\varepsilon$ and tan $\delta$ dispersion with a shifting of the dielectric maxima temperatures ($T_m$) towards higher temperatures with increase in frequency. The $T_m$ values of the dielectric spectra were fitted with a nonlinear Vogel–Fulcher (VF) relation (eqn (3)) as shown in the inset of Fig. 5(d).[37–39]

$$f = f_0 \exp\left(-E_a/k_B(T_m - T_f)\right) \quad (4)$$

where $f$ is the experimental frequency; $f_0$, the pre-exponential factor; $E_a$, the activation energy; $k_B$, the Boltzmann constant; and $T_f$, the static freezing temperature. The fitted parameters $E_a = 0.42$ eV, $f_0 = 5.48 \times 10^7$ Hz, and $T_f = 307$ K match the numerical values for other relaxor systems within the limit of their uncertainties.[37] The second phase transition is a diffused phase transition that fits well with the modified Curie–Weiss laws, as shown in Fig. 5(c).[37] The value of the diffusivity exponent, $\gamma \sim 1.78$ indicates that the system has broad dielectric relaxation and a higher level of disorder. The degree of disorder reveals that dynamic PNRs persist far above the lower phase transition temperature. The tangent loss illustrates a second anomaly below the second phase transition temperature that is normal for diffuse-type FE to PE phase transitions. It follows a similar trend of frequency response as that of the dielectric constant; however, the degree of tangent loss dispersion is very high (170–200 °C) compared to dielectric data near the 2nd phase transition. These observations favor high crystal disorder until the 2nd phase transition. One should note that the dielectric loss data and their dispersion with frequency and

 This journal is © The Royal Society of Chemistry 2014

Published on 07 April 2014. Downloaded by National Institute of Technology - Rourkela on 17/10/2014 07:27:03.

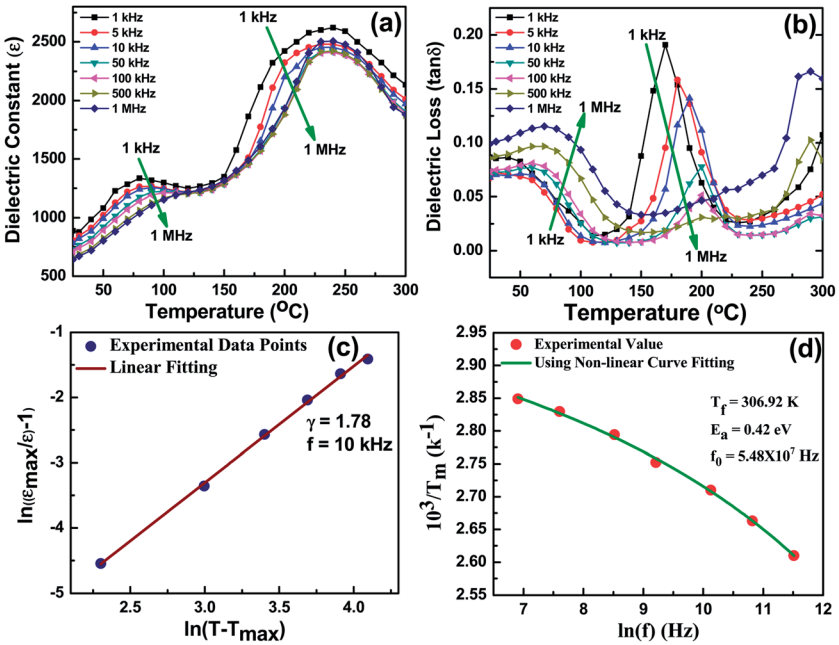


Fig. 5 Dielectric spectra (a) and tangent loss (b) as functions of temperature in the frequency range of (1 kHz–1 MHz), (c) non-linear VF relation fitting, (d) fitting of modified Curie–Weiss law near diffuse phase transition at 10 kHz.

temperature provide more reliable information than the dielectric constant values alone. The functional properties, variation in $T_m$ and dielectric loss depends on the probe frequency which is mainly due to the presence of short range ordering (SROs) such as PNRs or chemical inhomogeneity due to cation disordering in the long range order matrix. HRTEM images provide a clear picture that a large number of SROs, twin boundaries, discontinuous crystal planes, inhomogeneous distribution of A-site cations, *etc.* are present in the NBAT–BT matrix which in turn favors the dielectric dispersion and anti-polar properties.

### E. Polarization behavior under applied electric field

It has been described in previous studies that different kinds of dielectric material and their energy density capacity can be calculated from the *P–E* loop.[4–8] Among all dielectrics, relaxor–antiferroelectrics have shown the largest integrated area within their *P–E* loops to store energy efficiently. The relaxor–antiferroelectrics is the only system that possesses both nonlinear and linear *P–E* regions (except for temperatures slightly above $T_c$ in the first-order ferroelectrics); the linear antiferroelectric low-field region, the non-linear antiferroelectric region, and linear dielectric saturated region at extremely high field. The combination of nonlinear and linear *P–E* loops in the first quadrant of the *P*(*E*) hysteresis is suitable for high energy storage devices with a fast discharge capacity. Fig. 6(a) shows the slim relaxor–antiferroelectric hysteresis (as-grown samples) of the NBAT–BT system for a frequency of 1 Hz over a wide range of temperature. *P–E* loops for 1 and 10 Hz are given in the inset of Fig. 6(a) for a comparative study. These *P–E* loops become narrower and centered with an increase in temperature. Polycrystalline

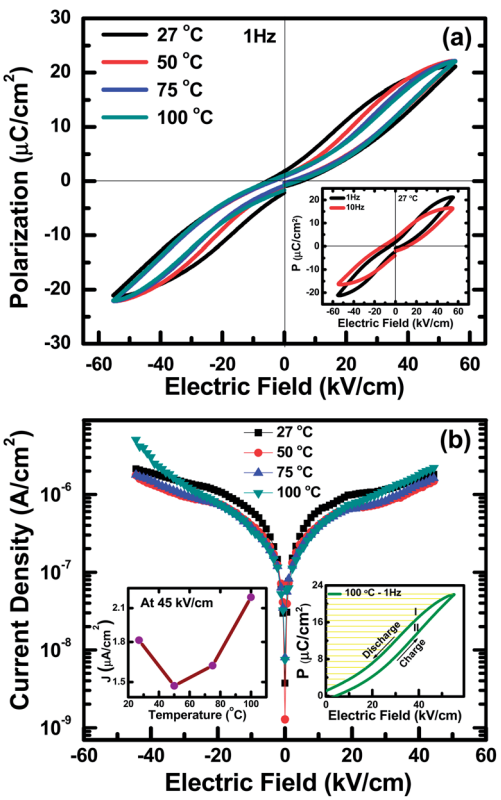


Fig. 6 (a) *P–E* loop hysteresis at different temperatures and a moderate applied electric field (50 kV cm$^{-1}$), in inset, *P–E* loops at 1 and 10 kHz for comparison. (b) Leakage current as a function of the applied electric field; right inset shows current density as a function of temperature. Shaded area (I) of *P–E* loop illustrates the capacity to store energy (left inset).

Published on 07 April 2014. Downloaded by National Institute of Technology - Rourkela on 17/10/2014 07:27:03.

ceramic samples are very prone to electrical breakdown under high electric field applications. We used a very moderate field ~50–60 kV $cm^{-1}$ to investigate the *P–E* loops to avoid large leakage current. Leakage current was separately measured for the same electric fields and was found to be a few μA. The magnitudes of these currents were at least three orders less than the range of real breakdown current (*ca.* mA) for insulating ceramics. It can also be seen from Fig. 5(b) that leakage current decreases with an increase in temperature which is a signature of the positive temperature coefficient of resistance (PTCR), extremely useful for power/energy based devices such as current-limiters.[40]

### F. Energy density capacity

The linear–nonlinear part of the *P–E* loop provides an energy density of ~0.4–0.6 J $cm^{-3}$ at 50 kV $cm^{-1}$ until 100 °C then increasing with increase in temperature and persisting above the $T_m$ of the relaxor–AFE phase transition. The shaded area in the inset of the *P–E* loop (Fig. 6(b)) represents the energy stored by the system. The *P–E* loops become narrower with increase in temperature, suggesting a high potential to store energy density. The inset of Fig. 6(b) shows two types (area I and II) of shaded areas (yellow and grey) that represent the charge and discharge capacities. Using *P–E* data, the discharge (release) ($U_d$), and charge ($U_c$) (storage) energy densities were calculated using the following relationship: $U_d$ = area II, $U_c$ = area I + area II. The charge–discharge efficiency ($\eta$) of the capacitors was calculated using the relationship: $\eta = U_d/U_c \times 100\%$. The efficiency of the NBAT–BT was 48% at 300 K for an applied electric field of 50 kV $cm^{-1}$. A similar range of efficiency was found for poly(vinylide fluoride–hexafluoropropylene) (PVDF–HFP).[41]

## Conclusions

In summary, relaxor-AFE lead-free NBAT–BT electroceramics were investigated for energy density applications. A small (~0.06%) substitution of $Al^{3+}$ cations in the NBAT–BT system near the MPB leads to the development of short range order polar nano regions within an AFE matrix. XRD analysis elucidates the coexistence of mixed rhombohedral and tetragonal phases. HRTEM images suggest the presence of disordered crystals, chemical inhomogeneity, and conjunction of nano-size crystals with larger grains. Two step-like phase transitions were seen in the dielectric and tangent loss spectra, which is characteristic of the relaxor–AFE to mixed AFE–FE phase at 80–120 °C, and the diffuse phase transition near 240 °C. The lower phase transition shows a large dielectric dispersion and follows a non-linear VF relation with freezing of PNRs at 34 °C. A pinched *P–E* hysteresis was observed over a wide range of temperature that clearly suggests the coexistence of the relaxor–AFE phase even far above the $T_m$. A moderate energy density and a low leakage current of 0.4–0.6 J $cm^{-3}$ and 1 μA were obtained at 50 kV $cm^{-1}$, respectively. These features suggest that lead-free relaxor–AFE ceramics or thin films have commercial potential for energy storage applications.

## Acknowledgements

The authors would like to acknowledge to Prof. J. F. Scott (Univ. of Cambridge, UK) for his critical evaluations and suggestions to improve the manuscript and Mr K. N. Sood for his support in carrying out SEM.

## References

1 S. A. Sherrill, P. Banerjee, G. W. Rubloff and S. B. Lee, *Phys. Chem. Chem. Phys.*, 2011, **13**, 20714.
2 C. A. Paz de Araujo, J. D. Cuchiaro, L. D. Mcmillan, M. C. Scott and J. F. Scott, *Nature*, 1995, **374**, 627.
3 B. Chu, X. Zhou, B. N. Kailiang Ren, M. Lin, Q. Wang, F. Bauer and Q. M. Zhang, *Science*, 2006, **313**, 334.
4 H. Ogihara, C. A. Randall and S. Trolier-McKinstry, *J. Am. Ceram. Soc.*, 2009, **92**(8), 1719.
5 G. R. Love, Energy Storage in Ceramic Dielectrics, *J. Am. Ceram. Soc.*, 1990, **73**(2), 323.
6 Z.-M. Dang, J.-K. Yuan, S.-H. Yao and H. Hong, *Adv. Mater.*, 2013, **25**, 6334.
7 N. Ortega, A. Kumar, J. F. Scott, D. B. Chrisey, M. Tomazawa, S. Kumari, D. G. B. Diestra and R. S. Katiyar, *J. Phys.: Condens. Matter*, 2012, **24**, 445901.
8 T. M. Correia, M. McMillen, M. K. Rokosz, P. M. Weaver, J. M. Gregg, G. Viola and M. G. Cain, *J. Am. Ceram. Soc.*, 2013, **96**(9), 2699.
9 J. Y. Li, L. Zhang and S. Ducharme, *Appl. Phys. Lett.*, 2007, **90**, 132901.
10 T. Takenaka, K. Maruyama and K. Sakata, *Jpn. J. Appl. Phys.*, 1991, **30**, 2236.
11 J. Rödel, W. Jo, K. T. P. Seifert, E.-M. Anton and T. Granzow, *J. Am. Ceram. Soc.*, 2009, **92**, 1153.
12 B. J. Chu, D. R. Chen, G. R. Li and Q. R. Yin, *J. Eur. Ceram. Soc.*, 2002, **22**, 2115.
13 Y. Guo, M. Gu, H. Luo, Y. Liu and R. L. Withers, *Phys. Rev. B: Condens. Matter Mater. Phys.*, 2011, **83**, 054118.
14 D. Maurya, V. Petkov, A. Kumar and S. Priya, *Dalton Trans.*, 2012, **41**(18), 5643.
15 V. Dorcet, G. Trolliard and P. Boullay, *Chem. Mater.*, 2008, **20**, 5061.
16 V. Dorcet, G. Trolliard and P. Boullay, *J. Magn. Magn. Mater.*, 2009, **321**, 1758.
17 C. Ma and X. Tan, *Solid State Commun.*, 2010, **150**, 1497.
18 C. Ma, H. Guo and X. Tan, *Adv. Funct. Mater.*, 2013, **23**, 5261.
19 T. Takenaka, K. Maruyama and K. Sakata, *Jpn. J. Appl. Phys.*, 1991, **30**, 2236.
20 I. W. Kim, D. S. Lee, S. H. Kang and C. W. Ahn, *Thin Solid Films*, 2003, **441**, 115.
21 C. Xu, D. Lin and K. W. Kwok, *Solid State Sci.*, 2008, **10**, 934.
22 Q. Xu, D.-P. Huang, M. Chen, W. Chen, H.-X. Liu and B.-H. Kim, *J. Alloys Compd.*, 2009, **471**, 310.
23 Y. S. Sung, J. M. Kim, J. H. Cho, T. K. Song, M. H. Kim, H. H. Chong, T. G. Park, D. Do and S. S. Kim, *Appl. Phys. Lett.*, 2010, **96**, 022901.

 This journal is © The Royal Society of Chemistry 2014

Published on 07 April 2014. Downloaded by National Institute of Technology - Rourkela on 17/10/2014 07:27:03.

24 S. Zhang, A. B. Kounga, W. Jo, C. Jamin, K. Seifert, T. Granzow, J. Rödel and D. Damjanovic, *Adv. Mater.*, 2009, **21**, 4716.
25 C. Ma and X. Tan, *J. Am. Ceram. Soc.*, 2011, **94**(11), 4040.
26 Y. Guo, M. Gu, H. Luo, Y. Liu and R. L. Withers, *Phys. Rev. B: Condens. Matter Mater. Phys.*, 2011, **83**, 054118.
27 K. Yao, S. Chen, M. Rahimabady, S. Yu, F. E. H. Tay, L. Lu, M. S. Mirshekarloo and T. Sritharan, *IEEE Trans. Ultrason. Ferroelectr. Freq. Control*, 2011, **58**, 1968.
28 P. Kim, N. M. Doss, J. P. Tillotson, P. J. Hotchkiss, M.-J. Pan, S. R. Marder, J. Li, J. P. Calame and J. W. Perry, *ACS Nano*, 2009, **3**, 2581.
29 V. Tomer, G. Polizos, E. Manias and C. A. Randall, *J. Appl. Phys.*, 2010, **108**, 074116.
30 S. Puli Venkata, A. Kumar, D. B. Chrisey, M. Tomazawa, J. F. Scott and R. S. Katiyar, *J. Phys. D: Appl. Phys.*, 2011, **44**, 395403.
31 W. Jo, J. E. Daniels, J. L. Jones, X. Tan, P. A. Thomas, D. Damjanovic and J. Rödel, *J. Appl. Phys.*, 2011, **109**, 014110.
32 D. T. Cromer, *J. Phys. Chem.*, 1957, **61**, 753.
33 R. S. Katiyar, J. F. Ryan and J. F. Scott, *Phys. Rev. B: Solid State*, 1971, **4**, 2635.
34 J. Suchanicz, I. J. Sumara and T. K. Kruzina, *J. Electroceram.*, 2011, **27**, 45.
35 M. Zhang, J. F. Scott and I. A. Zvirgds, *Ferroelectr., Lett. Sect.*, 1986, **6**, 147.
36 I. G. Siny, E. Husson, I. M. Beny, S. G. Lushnikov, E. A. Rogacheva and P. P. Syrnikov, *Phys. B*, 2001, **293**, 382.
37 H. Vogel, *Z. Phys.*, 1921, **22**, 645.
38 A. K. Tagantsev, *Phys. Rev. Lett.*, 1994, **72**, 1100.
39 I. Rivera, A. Kumar, N. Ortega, R. S. Katiyar and S. Lushnikov, *Solid State Commun.*, 2009, **149**, 172.
40 A. Kumar, R. S. Katiyar and J. F. Scott, *Appl. Phys. Lett.*, 2009, **94**, 212903.
41 S. Zhang and Q. Zhang, High energy density polymeric compositions, methods of the manufacture, and articles comprising the same, Patent no. US 2010/0067172 A1, 2010.